11-25-2019

Titanium and nitrogen interactions under laser additive manufacturing conditions

Congyuan Zeng
Louisiana State University

Hao Wen
Louisiana State University

Henry Bellamy
Louisiana State University

P. T. Sprunger
Louisiana State University

Paul J. Schilling
University of New Orleans

See next page for additional authors

Recommended Citation

Zeng, C., Wen, H., Bellamy, H., Sprunger, P., Schilling, P., & Guo, S. (2019). Titanium and nitrogen interactions under laser additive manufacturing conditions. *Surface and Coatings Technology, 378* https://doi.org/10.1016/j.surfcoat.2019.124955

Surface & Coatings Technology 378 (2019) 124955

Contents lists available at ScienceDirect

Surface & Coatings Technology

journal homepage: www.elsevier.com/locate/surfcoat

Titanium and nitrogen interactions under laser additive manufacturing conditions

Congyuan Zeng[a], Hao Wen[a], Henry Bellamy[b], P.T. Sprunger[b,d], Paul J. Schilling[c], S.M. Guo[a,*]

[a] Department of Mechanical & Industrial Engineering, Louisiana State University, Baton Rouge, LA 70803, United States
[b] The J. Bennett Johnston, Sr. Center for Advanced Microstructures and Devices, LSU, Baton Rouge, LA 70803, United States
[c] Department of Mechanical Engineering, University of New Orleans, New Orleans, LA 70148, United States
[d] Department of Physics & Astronomy, Louisiana State University, Baton Rouge, LA 70803, United States

ARTICLE INFO

Keywords:
Titanium nitridation
Laser melting
in-situ phase transformation
Synchrotron X-ray diffraction

ABSTRACT

To understand how to make bulk titanium parts or coatings with desired levels of titanium nitrides, this paper investigates the dynamic interactions between titanium and nitrogen under representative laser-based additive manufacturing (AM) conditions. Under a set of gas environments containing different concentrations of nitrogen, the titanium and nitrogen reaction products—formed under typical Selective Laser Melting (SLM) and Laser Engineered Net Shaping (LENS) AM scanning conditions—are examined for compositions, phases, and microstructures. *In-situ* synchrotron X-ray diffraction (SXRD) test is performed to reveal the high temperature reaction steps between titanium and nitrogen.

1. Introduction

Laser-based additive manufacturing (AM) enables the manufacturing of complex shaped metallic products. At present, there are two main types of laser-based AM processes: 1) Laser Powder Stream, or LENS®-Laser Engineered Net Shaping™ [1–4], developed by Sandia National Laboratories; and 2) Laser Powder Bed Fusion based process, such as Selective Laser Melting (SLM) [5–8]. SLM has the advantage of high precision while LENS has the advantage of free forming capability. According to Frazier's study [9], the size of the melt pool for the LENS process is typically one order of magnitude larger than that of SLM process, because the laser scanning speed (and in turn the cooling rate) for the LENS process is much less than that of the SLM process. Due to its excellent properties, such as good corrosion resistance, biocompatibility, and high strength-weight ratio, Ti has been widely used for biomedical and aerospace applications [10,11]. Using laser-based AM, complex shaped Ti/Ti-ceramic particle composite parts can be produced with improved mechanical properties [12–14].

It's well known that Ti reacts with nitrogen (N_2) at elevated temperatures. As the maximum temperature under laser irradiation in AM processes could be as high as 2400 °C [15], titanium nitride is expected to form if N_2 is present. To reduce the tendency of nitride formation in the laser AM processes, the processing chamber of a laser AM machine is typically purged with Argon (Ar). Taking a typical SLM system as an example, the residual oxygen (O_2) concentration is usually set to be below 0.1% before the laser AM process starts. However, for certain applications, Ti alloy parts are deliberately processed to form a nitride coating in a laser nitridation process [16,17]. Mridha and Baker [18] studied laser nitridation on Ti-4V-6Al (Ti64) samples under a pure N_2 gas-flow environment and found that the concentration of nitride dendrites on sample surfaces increased with the increase of N_2 gas flow and laser energy density; Razavi et al. [19] reported that after laser nitridation on Ti64 surfaces under a pure N_2 environment, titanium nitride layer was produced, and the corrosion resistance of the coated Ti64 in HCl solution was enhanced; Man et al. [20] investigated laser diffusion nitridation on Ti64 with different laser powers and laser scanning speeds for improved hardness and wear resistance. With a slow laser scanning speed, ranging from a few to tens of millimeters per second commonly found in the LENS process, a thick titanium nitride coating (about tens of microns) can be formed for tribological applications [21]. Kazantseva et al. [22] reported that the microstructure of such a nitride coating layer had a pure TiN layer on top of a mixed layer where hard TiN dendrites were embedded in the Ti matrix. Under a fast scanning rate, the nitridation process is expected to be incomplete. For example, Dahotre et al. [23] examined Ti surfaces partially covered with TiN coatings for improved osseo-integration performance, where the reported TiN volume fraction was generally less than 10%.

As previous laser nitridation studies are mainly focused on the formation of thick titanium nitride layers [18–22], very little work has been conducted on the early stage of nitride formation under laser AM

* Corresponding author.
E-mail address: sguo2@lsu.edu (S.M. Guo).

https://doi.org/10.1016/j.surfcoat.2019.124955
Received 31 July 2019; Received in revised form 1 September 2019; Accepted 4 September 2019
Available online 04 September 2019

conditions. To understand how to make bulk titanium parts or coatings with desired levels of titanium nitrides using AM, this study investigates the dynamic reactions between Ti and N_2 under different laser AM processing conditions.

2. Materials and methods

2.1. Nitridation process under a slow laser scanning speed and In-situ synchrotron X-ray diffraction test

The purpose of this test is to find out the high temperature reaction steps for Ti in a N_2 environment under a slow laser scanning speed. A commercially pure Ti piece $16 \times 13 \times 3\,mm^3$ with 99.2 wt% purity was used as the target. Pure N_2 (ultrahigh purity 5.0 grade) was applied as the alloying gas. An IPG YLS-2000 fiber laser (with a maximum power of 2000 W) was utilized as the heating source to mimic the LENS process. The *in-situ* SXRD test was conducted on the Protein Crystallography synchrotron beamline at the Center for Advanced Microstructures and Devices (CAMD), Baton Rouge, Louisiana, USA. This facility has a 1.3 GeV electron storage ring that is built exclusively to provide synchrotron radiation. In this study, X-ray with a wavelength of 1.3808 Å was used, and the X-ray beam size was adjusted to 0.3 mm*0.3 mm using slits. A PILATUS 100 K (Dectris AG, Switzerland) detector system, with a maximum framing rate of 100 Hz, was used for logging the diffraction data. Synchrotron diffraction satisfies the Bragg's equation, $2dsin\theta = \lambda$, where d is interplanar spacing, 2θ is diffraction angle and λ is the wavelength of synchrotron X-rays. The program FIT2D was used to integrate the sequential data files, taken during the transient laser heating/solidification process, into one frame to give diffraction angles and intensity information of the whole process.

The schematic configuration of the *in-situ* SXRD test setup is shown in Fig. 1. A defocused laser beam with a spot size of around 0.8 mm is used. The synchrotron X-ray beamline interacts with the sample surface region corresponding to the laser spot. An inclination angle of 20° is set between the sample surface and the incident synchrotron X-ray, to achieve an effective X-ray-sample interaction. The irradiation power of laser is programmed to generate localized melting and solidification suitable for *in-situ* SXRD testing. The PILATUS 2D detector collects the diffraction angles, for example δ and γ shown in Fig. 1, and diffraction intensities to reveal the reactive process.

For the sample setup, the Ti piece is placed on top of an aluminum sample holder. To avoid slippage of the sample piece, an adhesive bond is applied. Before testing, a N_2 purging flow is used to keep the targeted laser irradiation area in a N_2 atmosphere. After the synchrotron X-ray beam is applied, the detector initiates data recording at a framing rate of 10 Hz. After about 1 s, laser power is applied. The laser power changes to 200 W from 0 W with a constant rate of 40 W/s. The maximum power of 200 W is kept for 1 s before the power is reduced back to 0 W with a constant rate of −200 W/s. After bringing the laser power back to 0 W, X-rays and detector are applied for additional 3 s. This represents a very slow laser scanning process.

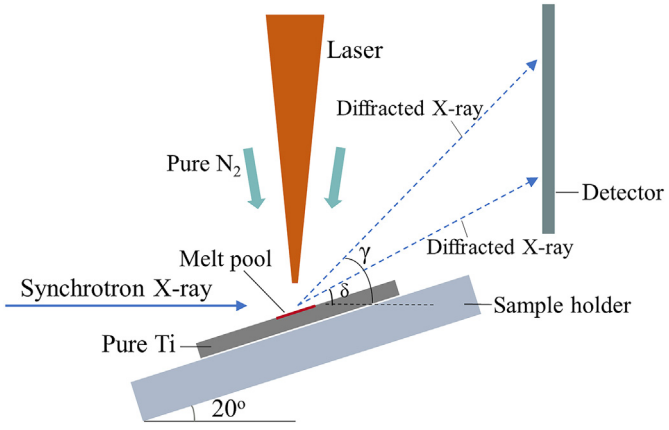

Fig. 1. Schematic of the synchrotron X-ray diffraction setup.

2.2. Nitridation process under SLM representative conditions

ThermoCalc™ software is used to generate the Ti—N binary phase diagram utilizing the TCBIN database. To subject Ti samples under different laser processing parameters and N_2 gas environments, a custom SLM device is used. This custom SLM system has a 200 W IPG ytterbium fiber laser with a wavelength of 1064 nm. A ProSeries II scan head is used to control the scan patterns. A JENar F-Theta lens can reduce the laser spot size to 46 μm at the focal plane. Laser power is fixed at 175 W in the study. Different scanning speeds result in different melt pool sizes and theoretically lead to different cooling rates. The scanning speeds selected in the study are 25, 100, 400 and 1600 mm/s. Six different N_2 contents, namely 0%, 5%, 20%, 50%, 75% and 100%, with the balance of Ar, are selected to examine the impact of N_2 concentration on the nitridation process. The pressure of the N_2/Ar gas mixture is kept at 1 atm.

2.3. Sample characterizations

The phases, compositions, and microstructures of the prepared samples under the above-mentioned laser scanning parameters and gas environments are characterized. To reveal the cross sections of molten tracks, a BUEHLER low-speed saw is used to section the samples, followed by grinding using *SiC* papers with the sizes 320, 600, 800, 1000 grit sequentially. The surfaces are subsequently polished with diamond suspension (MetaDi™ Supreme polycrystalline, 1 μm), followed by ultrasonic rinsing in acetone, ethanol, and deionized water for 20 min each. Finally, the polished cross sections are etched using the Kroll's Reagent purchased from PACE Technologies. A Quanta™ 3D DualBeam™ FEG FIB-SEM scanning electron microscope (SEM) is utilized to observe the microstructures of the laser processed areas, including the measurements of the molten track geometries. PANalytical X-ray diffraction (XRD) is used to analyze phases of laser scanned surfaces. Based on the intensities of the strongest diffraction peaks and the Reference Intensity Ratio (RIR) value obtained from the standard powder diffraction file (PDF) cards, the amounts of all phases can be calculated using the following equation $w_x = I_x/(K_x(I_1/K_1 + I_2/K_2 + \ldots + I_x/K_x))$, where w, I and K are mass fraction, diffraction intensity of the strongest peak and RIR value, respectively, and the subscripts indicate different phases. Kratos AXIS 165 X-ray photoelectron spectroscopy (XPS) is applied to test surface compositions. In the XPS tests, Ar^+ sputtering is applied to remove contaminants from the sample surfaces.

3. Results and discussions

Different laser nitridation conditions, to mimic both LENS and SLM laser AM conditions, are applied onto Ti samples under different N_2 environments. The resulting phases, compositions, and microstructures of laser-scanned surfaces are discussed below.

3.1. Dynamic interaction process of Ti and N_2 using in-situ SXRD

Fig. 2 shows the SXRD results analyzed by software FIT2D, which gives the variation of diffraction angles and intensities as a function of frame number (time). In this test, a 10 Hz sampling rate is applied. Therefore, the y-axis, with a total of 120 frames, gives the indication of time from zero to 12 s. The initial time zero is arbitrarily set to be about 1 s before the laser heating. As shown in Fig. 2, the Ti and N_2 interactions can be divided into four stages.

Stage 1 (y = 0–10 and 10–28) shows the diffraction angles and intensities at around room temperature (RT), which reveals the

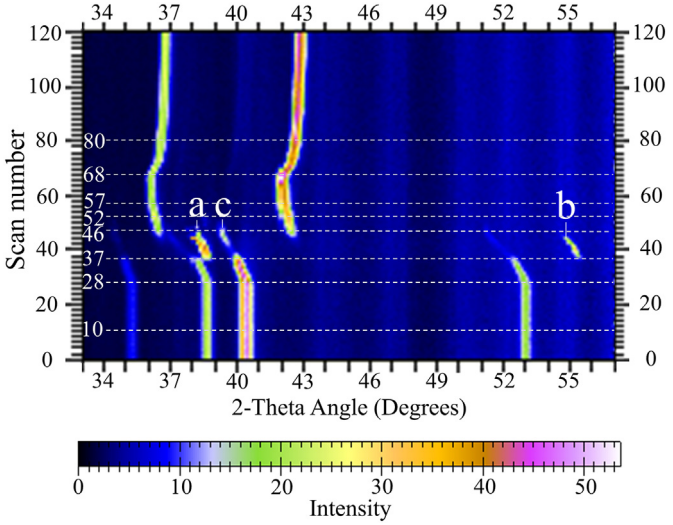

Fig. 2. *In-situ* diffraction angle and intensity as a function of time, a, b represent the diffraction peaks of β-Ti, c is the diffraction peak of α-Ti.

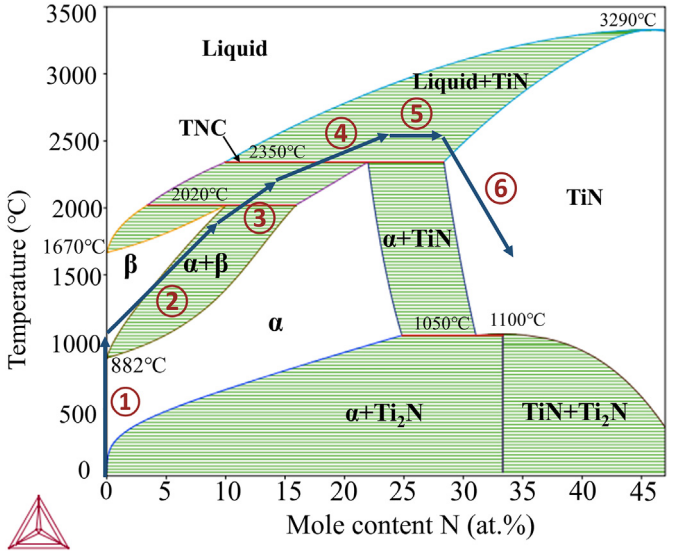

Fig. 3. Titanium-nitrogen phase diagram. Phase transformation process ① αTi → βTi. ② βTi → αTi + βTi. ③ αTi + βTi → liquid + αTi. ④ Liquid + αTi → liquid + TiN. ⑤ Liquid + TiN. ⑥ Liquid + TiN→solid + TiN.

diffraction patterns belong to pure Ti. Stage 1 can be further divided into two periods, time frames from 0 to 10 (period 1) and time frames from 10 to 28 (period 2). In period 1, before laser initiation, the sample stays at RT. At frame 10, laser irradiation is initiated. During period 2, the laser power increases linearly from 0 to 72 W. The change of laser power does not cause a noticeable shift of XRD peaks during this period.

Stage 2 (y = 28–37 and 37–46) is the temperature rising period for the Ti sample under laser irradiation. In this step, diffraction peaks continuously shift to the lower 2θ value side (frames 28 to 37). According to Bragg's equation, $d = \lambda/(2dsin\theta)$, decrease of θ indicates an increase of the interplanar spacing, d, value. For close-packed hexagonal (HCP) crystals, such as α-Ti in this period, the relationship between interplanar spacing and lattice parameters is $d = 1/\sqrt{4(h^2 + hk + k^2)/3a^2 + 1/c^2}$, where h, k and l are miller indices, while a and c are lattice parameters for HCP crystals. For cubic space groups, for example β-Ti and TiN generated later, the d value is directly proportional to lattice parameter, a, and the relation between them can be described as $a = d\sqrt{h^2 + k^2 + l^2}$. According to the relationships mentioned above, the increase of lattice parameters leads to an increase of interplanar spacing, and the decrease of lattice parameters results in a decrease of interplanar spacing. With the progress of laser irradiation, the temperature of the Ti sample increases, which leads to the sample expansion. If both temperatures and diffraction angles are precisely measured, *in-situ* thermal expansion can then be calculated. At around frame 37, the Ti sample reaches a critical temperature from laser irradiation. At this temperature, abrupt changes of diffraction angles and intensities occur due to phase change. When the temperature reaches about 882 °C, pure Ti transforms from HCP structure, αTi, to body-centered cubic (BCC) structure, βTi [24]. The points a and b in Fig. 2 correspond to diffraction peaks of βTi. Point c in Fig. 2 shows the regeneration of αTi, because it lies on the extension line of former αTi diffraction patterns. Based on Fig. 2, although there is an abrupt change in diffraction intensity when reaching the phase transition time frame, weak diffraction peaks of αTi can still be detected. The αTi signal becomes even stronger at around time frames 40 to 46, point c, which indicates an increase of αTi in the sampled region. For pure Ti, a direct transition from αTi to βTi is expected. The coexistence of the α and β phases is interpreted as an indication of the presence of nitrogen in the structure. According to the Ti—N phase diagram in Fig. 3 calculated by ThermoCalc™ software, with the increase of temperature, nitrogen solubility in Ti increases dramatically. Also, with laser irradiation under a N_2 environment, nitrogen plasma can be induced by the laser, which is evidenced by the work of Wang et al. [25], facilitating the diffusion of nitrogen into Ti, and increasing nitrogen concentration in the Ti substrate. The pure Ti sample first experiences the α to β phase transition at time frame 37. With the rapid nitrogen intake at the elevated temperatures, the increased nitrogen content brings the system into the α + β two-phase area. When temperature continues to increase, dissolution of nitrogen into the Ti substrate is accelerated, and more αTi is formed from βTi. That is why enhanced intensity can be observed around point c in Fig. 2 over frames 40 to 46. With the further increase of temperature and nitrogen concentration, the βTi melts or converts to αTi, and TiN starts to form rapidly. Most of Ti enters Liquid + αTi two-phase region and small amount of Ti reaches Liquid + TiN two-phase area. The coexistence of αTi and TiN is clearly identified by the *in-situ* SXRD test at frame 46. One explanation could be the uneven temperature distribution over the area illuminated by the X-rays. The laser beam has a Gaussian distribution, where the center of the laser beam has a higher power density. Therefore, the Ti surface area that interacted with the laser spot center has a higher temperature, thus the Liquid + TiN two-phase area would occur first at the center of the laser illuminated area. With a further increase of temperature and more progress of nitridation, the surface TiN layer becomes thick enough to dominate the synchrotron X-ray diffraction pattern.

Stage 3 (y = 46–52, 52–57, and 57–68) Time frames 46 to 52 indicate a TiN layer floating on a molten Ti. In this period, the temperature becomes even higher as the TiN diffraction patterns further move toward smaller angles. In the meantime, more nitrogen is absorbed and reacted with liquid Ti, causing the diffraction intensity of TiN to be further enhanced. For time frames 52 to 57, a further increase of temperature is observed from the shift of the TiN diffraction patterns. However, the TiN diffraction intensity remains almost constant. This could be due to the reduced nitrogen diffusion through an already thickened TiN layer. From time frames 57 to 68, there is little diffraction angle shift in this stage, which indicates that with the laser processing profile used in this study, the temperature of the molten spot stays constant as the laser irradiation power is balanced with heat losses due to radiation and conduction.

Stage 4 (y = 68–80) is the solidification process. Based on Fig. 2, apparently, similar with stage 3, only TiN diffraction peaks can be detected and no new phases are generated. Diffraction peak shifts can also be observed, which is due to contraction during the cooling down stage.

To sum up, based on the *in-situ* SXRD results, diffraction peak shifts

can be detected during both the heating and the cooling process. Based on the shift of the diffraction angles, an *in-situ* coefficient of thermal expansion could be calculated if the sample temperature could be measured. With a slow laser scanning speed, thus a long laser dwelling time, a complete TiN layer can be formed. The nitridation process happens rapidly once the temperature is near the Ti melting point. Within 0.6 s (time frames 46 and 52), a thick TiN layer is formed. According to the research of Valvoda and Musil [26], the thickness of the TiN layer is estimated to be about 5.5 μm. Considering the synchrotron X-ray used in the study, 8980 eV, the attenuation length in solid TiN is about 16 μm. Based on the diffraction setup, when the continuous TiN layer thickness reaches 5.5 μm, only TiN signal should be detected. During the Ti−N_2 interactions, the surface of Ti sample underwent the following phase change process, $\alpha Ti \rightarrow \beta Ti \rightarrow \alpha Ti + \beta Ti \rightarrow liquid + \alpha Ti \rightarrow liquid + TiN \rightarrow solid + TiN$.

3.2. Effect of laser scanning speed on phases, compositions, and microstructures of Ti under N_2 environments

3.2.1. The laser processing parameters and the resulting molten tracks

Ti samples are processed using a custom SLM system with a laser power of 175 W. To quantify the molten track geometries, a single laser scanning track is performed under each scanning speed on pure Ti samples. The processing chamber of the SLM system is first evacuated down to 145 Pa, and then refilled with pure Ar to 1 atm. Fig. 4 shows a set of laser track widths under different scanning speeds and the cross-section morphology of melt pool processed with the laser scanning speed of 25 mm/s. According to Fig. 4(a), (b), (c) and (d), with the increase of scanning speed, the width of the laser track decreases, and the detailed results are listed in Table 1. The ripple lines on the molten track become elongated along the laser scanning direction with the increase of scanning speed. To observe the cross sections of the scanning tracks, samples are cut, grinded, and polished, followed by a chemical etching process. The SEM image of an etched cross section is shown in Fig. 4(e), revealing a semi-elliptical shaped melt pool. The ratio of the melt pool width to depth varies from 4.5:1 to 5:1, which indicates a conduction mode of laser processing [27]. The shallow penetration depth of laser melting is resulted from the large spot size of the laser on Ti surfaces, which significantly reduces the laser power density. By measuring the single laser scanning track melt pool geometries, the hatch spacing under each laser scanning speed is determined to form at least 50% overlapping to achieve a full molten track coverage of the processed sample surfaces, Table 1.

Table 1
Melt pool sizes and the determined hatch spacing under different scanning parameters.

Parameter	Value			
Laser power (W)	175	175	175	175
Spot size (μm)	207	207	207	207
Scanning speed (mm/s)	25	100	400	1600
Width of melt pool (μm)	473	252	151	75
Depth of melt pool (μm)	93	55	34	16
Hatch spacing (μm)	230	120	64	35

3.2.2. Effect of different laser scanning speeds on phases and composition of Ti under N_2 environments

Based on the laser processing parameters listed in Table 1, Ti samples are prepared with four different scanning speeds, 25, 100, 400 and 1600 mm/s, in pure N_2 atmosphere. Fig. 5 shows the XRD results and phase composition of the samples. Based on Fig. 5(a), in addition to pure Ti, titanium nitrides, namely TiN and $TiN_{0.26}$, are also detected on the surfaces of all four samples. However, it is also obvious that with the increase of scanning speed, diffraction peak intensities of titanium nitride are decreased. For example, the intensity ratio of the strongest diffraction peak of TiN (at the diffraction angle ~43°) to that of Ti (at the diffraction angle ~40°) decreases continuously, indicating the reduced amount of titanium nitride. Fig. 5(b) shows the relation between

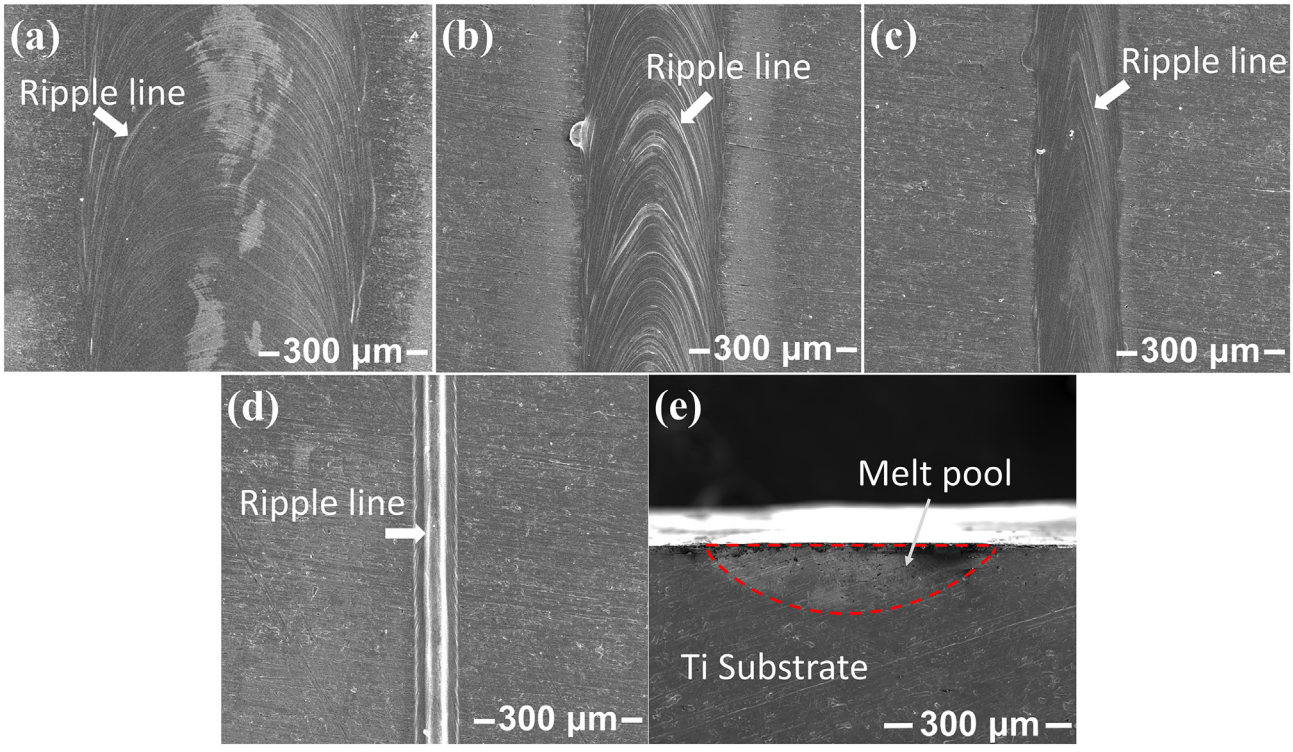

Fig. 4. Images showing the widths of laser molten tracks with different scanning speeds (laser power 175 W, laser spot size 207 μm) and melt pool cross section morphology. The single tracks are processed with laser scanning speeds (a) 25 mm/s (b) 100 mm/s (c) 400 mm/s (d) 1600 mm/s. (e) shows the cross-section morphology of the sample processed with the scanning speed of 25 mm/s.

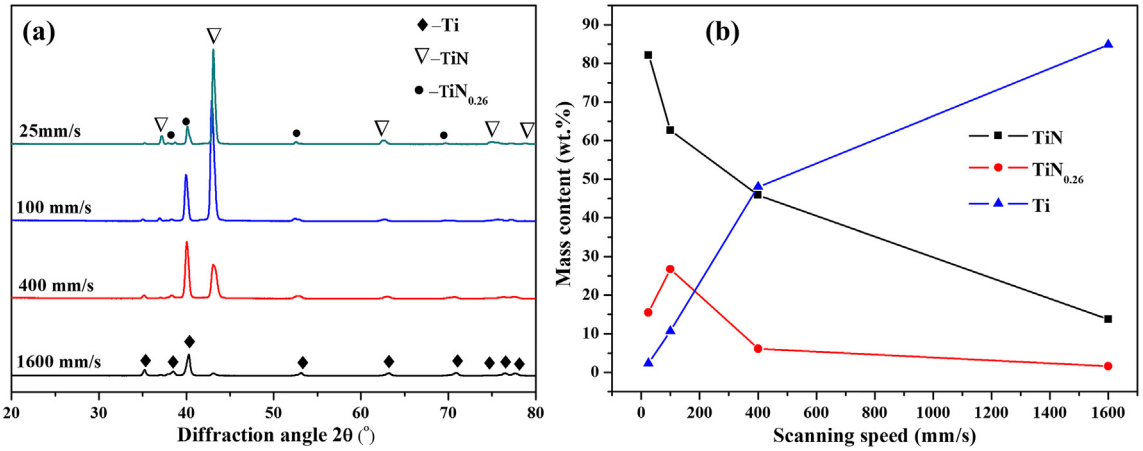

Fig. 5. Images displaying XRD results and phase compositions of the samples. (a) shows the XRD results of the samples processed under different scanning speeds with a laser power of 175 W and a laser spot size of 207 μm in a pure N_2 environment. (b) shows the phase composition information on the surfaces of the samples aforementioned according to XRD results.

the calculated mass content of three different phases (Ti, TiN and $TiN_{0.26}$) under different scanning speeds. When the scanning speed increases from 25 mm/s to 1600 mm/s, the content of TiN and $TiN_{0.26}$ decreases from 82.2% to 13.7% and from 15.5% to 1.6%, respectively, while the mass content of Ti increases from 2.3% to 84.8%.

The scanning speeds of 25 mm/s and 100 mm/s represent the LENS process, while the scanning speeds of 400 mm/s and 1600 mm/s match the SLM process better. Clearly, nitridation can still be observed with a fast scanning speed, for example 1600 mm/s in this study, if a SLM system uses pure N_2 in the processing chamber. Under SLM conditions, laser-sample interaction time is an order of magnitude shorter than that of the LENS process. Within the limited laser-sample interaction time, the temperature of the laser-sample interaction spot may not be as high as that of LENS case. The combination of a shortened interaction time and a low temperature results in a thin and discontinuous titanium nitride layer. For the LENS method, taking the laser scanning speed of 25 mm/s and a melt pool size of 0.5 mm, a layer with more than 80% TiN could be formed under a dwelling time of 20 ms.

3.3. Effect of controlled N_2 atmospheres on phases and composition of Ti samples

The effects of controlled N_2 atmospheres on the phases and compositions of Ti samples prepared under representative SLM conditions are studied. Controlled N_2 atmospheres selected in the study are 0%, 5%, 20%, 50%, 75% and 100% of N_2 concentration with balance gas Ar. Parameters listed in Table 1 are applied to prepare samples. Based on XRD results, Fig. 6(a), with 100% N_2, diffraction peaks of TiN can be clearly seen. However, when N_2 content is below 75%, diffraction peaks of TiN can hardly be observed, which indicates remarkably low titanium nitride content on sample surfaces. The relation between the titanium nitride mass content obtained from the XRD analysis and the N_2 gas content is plotted in Fig. 6(b). Evidently, when N_2 content is decreased, less TiN will be generated on the sample surfaces. When N_2 is at low content, from 0% to 50%, TiN and $TiN_{0.26}$ concentrations are negligible. When N_2 content is increased from 50% to 75%, a slight increase of the amount of TiN and $TiN_{0.26}$ is observed, increasing from 0.2% to 3.6% and from 0% to 0.7%, respectively. A sharp increase of the amount of titanium nitrides is observed with 100% N_2, with the amounts of TiN and $TiN_{0.26}$ up to 45.9% and 6.1%, respectively. This demonstrates the significant influence of N_2 content on the formation of titanium nitride during the laser AM processes.

3.4. Surface composition test for samples made under controlled N_2 atmosphere by XPS

To obtain more accurate element content of laser scanned surfaces under controlled N_2 atmospheres, X-ray photoelectron spectroscopy (XPS) method is applied. Different from XRD, detection depth of XPS is typically within 10 nm. For comparison, XRD detection depth is typically in the order of several micrometers. Therefore, XPS gives the outermost surface composition information of a sample, while XRD gives the average composition information with a depth of several micrometers. As Ti is an active element, it reacts with O_2 even at RT when exposed to air. Ar^+ sputtering is applied to remove surface contaminants, especially titanium oxides, in the XPS testing.

Fig. 7(a) shows the relation between the element content on the sample surfaces and the Ar^+ sputtering time. The sample examined here is prepared under 100% N_2 atmosphere. As the sputtering time is increased, the Ti content increases continuously. O content decreases rapidly from 63% to 15% when the sputtering time is increased from 0 min to 20 min. However, when the sputtering time is further increased from 20 min to 60 min, O content reduces from about 15% to 8% at a much slower rate. In the meantime, N content increases from about 8% to 32% with a sputtering time of 20 min. The increase of N content and the sharp decrease of O content indicate that the O presents mainly on the sample outermost surface. When the sputtering time is increased to 40 min and 60 min, the N content has little change (26% to 23%). As the N content is the research focus, the sputtering time is chosen to be 20 min.

Fig. 7(b), (c), (d) and (e) show XPS survey scan spectra of the sample prepared under 100% N_2 atmosphere after Ar^+ sputtering for 20 min. Fig. 7(b) is a full range XPS scan spectra, which reveals the coexistence of Ti, N, and O. Fig. 7(c), (d) and (e) are narrow scans of Ti, N, and O, respectively. Refer to the work of Biesinger et al. [28], it is discovered that Ti mainly exists in the form of TiN, Ti^{3+} (e.g. Ti_3O_2), and Ti^{2+} (e.g. TiO). No TiO_2 is detected, which might result from the fact that the outermost surface has been removed during the Ar^+ sputtering process. N is found to exist in two forms according to N narrow-range XPS scan spectra, which is consistent with the XRD results, where two titanium nitrides, TiN and $TiN_{0.26}$, are detected.

For samples prepared under different N_2 concentrations during the laser scanning process, after 20 min Ar^+ sputtering, the sample surfaces are XPS tested to obtain elemental composition information, Fig. 7(f). Clearly, Ti content and N content have adverse variation behaviors. Overall, Ti content decreases with the increase of N_2 concentration, while N content increases. In the meantime, O content stays almost the same (with a narrow range from 12% to 16%) over the entire N_2

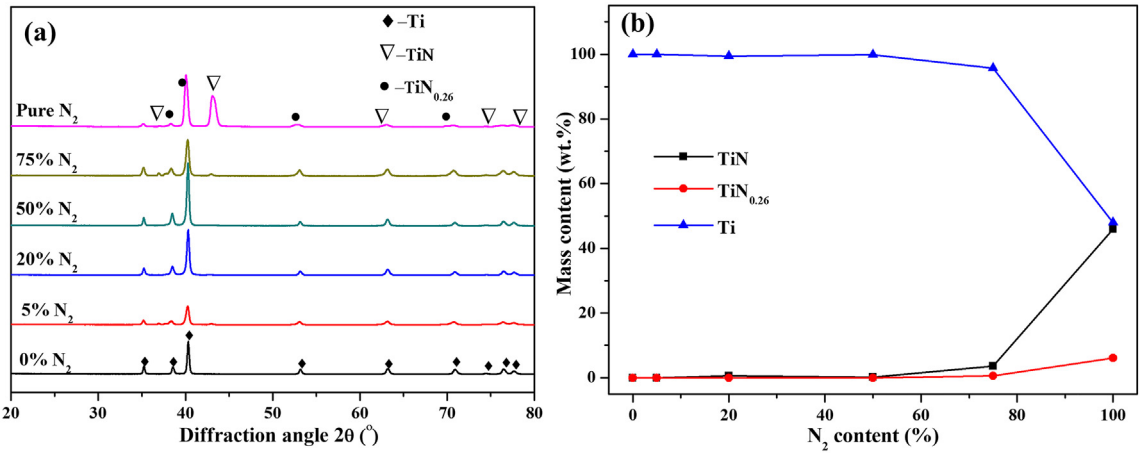

Fig. 6. Images showing XRD results and phase compositions of the sample surfaces. (a) exhibits the XRD results of the samples processed under controlled N_2 atmospheres (laser power 175 W, laser spot size 207 μm, and a scanning speed of 400 mm/s), (b) demonstrates the phase composition information on the surfaces of the corresponding samples based on XRD test results.

concentration range. Most likely, the oxygen element comes from the reaction between Ti and the trace amount of O_2 in both N_2 and Ar gas used in the research. When N_2 content is less than 50%, N, Ti, and O contents on the sample surfaces remain basically the same. As N_2 content in the chamber is increased further from 50% to 75%, a clear increase of N content occurs, from 5% to 25%. Meanwhile, Ti content dropped from 78% to about 60%. When N_2 content goes up to 100%, N content reaches the maximum value of 32%, while Ti content achieves the minimum value of 52%. The variation behavior of N content detected by XPS is consistent with the results obtained from XRD test shown in Fig. 6(b). However, some difference for the sample made under 75% N_2 atmosphere is observed. For the 75% N_2 atmosphere case, N content detected by XPS is much higher than that obtained by XRD, due to the detection depth difference between XPS and XRD. By controlling N_2 atmosphere, controlled compositions and phases on titanium surfaces can be obtained with SLM conditions.

4. Conclusions

This paper investigates the dynamic interactions between Ti and N_2 under laser-based AM conditions. The dynamic reaction process of Ti and N_2 under a slow laser scanning speed, mimicking the LENS method, is examined using *in-situ* SXRD. The nitridation products, prepared under representative LENS and SLM laser scanning speeds and controlled N_2 atmospheres, are examined for phase compositions and microstructures. The following conclusions are reached.

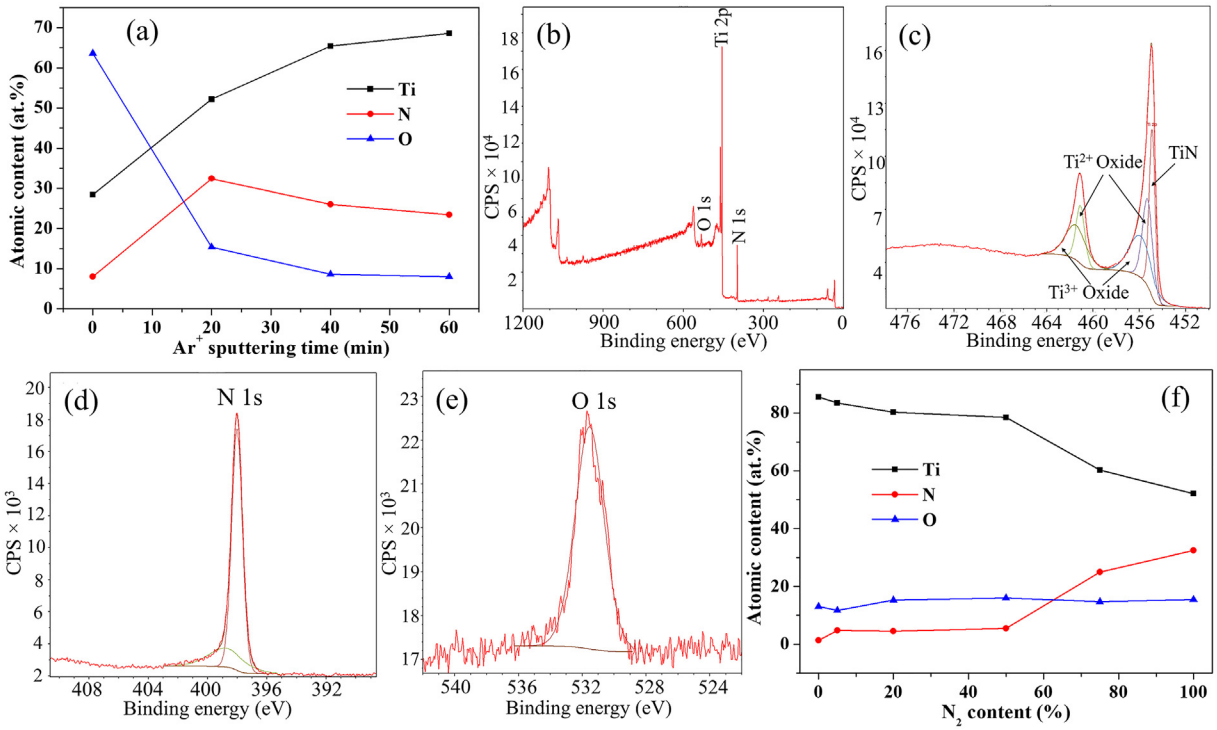

Fig. 7. (a) Shows the relation between surface element composition and Ar^+ sputtering time for the sample processed under 100% N_2 atmosphere. (b), (c), (d) and (e) display the XPS survey scan spectra of sample surface, processed under 100% N_2 atmosphere, after 20 min Ar^+ sputtering, with (b) full range scan spectra, and narrow scan spectra of (c) Ti, (d) N, and (e) O. (f) demonstrates the relation between sample surface composition and controlled N_2 atmosphere. All the samples tested here were processed with laser power 175 W, laser spot size 207 μm, and a scanning speed of 400 mm/s.

(1) According to the SXRD test, high temperature reactions steps between Ti and N_2 are clearly identified. Referring to the Ti—N binary phase diagram, phase transformations during the laser process can be described as $\alpha Ti \rightarrow \beta Ti \rightarrow \alpha Ti + \beta Ti \rightarrow liquid + \alpha Ti \rightarrow liquid + TiN \rightarrow solid + TiN$.
(2) Within a pure N_2 environment, the time to form a thick TiN layer to blocked synchrotron X-ray penetration on molten titanium is approximately 0.6 s.
(3) Two titanium nitrides, namely TiN and $TiN_{0.26}$, are identified under laser AM processing conditions. With the increase in scanning speed, the content of titanium nitride decreases.
(4) Nitrogen content on sample surfaces increases with the increase of N_2 content in the processing chamber under the same laser processing parameters. When N_2 content is below 50%, nitrogen content on sample surface stays at a low level of under 5% based on XPS results. When N_2 content increases from 50% to 100%, nitrogen intake on the Ti surface jumps up quickly to a high level of about 30%. Further studies on mechanical properties for samples prepared under different N_2 content are worth pursuing.

Acknowledgements

This work was supported by the National Science Foundation-Consortium for innovation in manufacturing and materials (CIMM) program (grant number # OIA-1541079), USA. HB is partially supported by the Louisiana Governor's Biotechnology Initiative.

References

[1] H. Attar, S. Ehtemam-Haghighi, D. Kent, X. Wu, M.S. Dargusch, Comparative study of commercially pure titanium produced by laser engineered net shaping, selective laser melting and casting processes, Mater. Sci. Eng. A 705 (2017) 385–393.
[2] I. Kunce, M. Polanski, K. Karczewski, T. Plocinski, K.J. Kurzydlowski, Microstructural characterisation of high-entropy alloy AlCoCrFeNi fabricated by laser engineered net shaping, J. Alloys Compd. 648 (2015) 751–758.
[3] Z. Fan, Y. Zhao, Q. Tan, N. Mo, M.-X. Zhang, M. Lu, H. Huang, Nanostructured Al_2O_3-YAG-ZrO_2 ternary eutectic components prepared by laser engineered net shaping, Acta Mater. 170 (2019) 24–37.
[4] V.K. Balla, A. Bandyopadhyay, Laser processing of Fe-based bulk amorphous alloy, Surf. Coat. Technol. 205 (2010) 2661–2667.
[5] N. Read, W. Wang, K. Essa, M.M. Attallah, Selective laser melting of $AlSi_{10}Mg$ alloy: process optimisation and mechanical properties development, Mater. Des. 65 (2015) (1980-2015) 417–424.
[6] K.G. Prashanth, S. Scudino, J. Eckert, Defining the tensile properties of Al-12Si parts produced by selective laser melting, Acta Mater. 126 (2017) 25–35.
[7] G. Kasperovich, J. Hausmann, Improvement of fatigue resistance and ductility of $TiAl_6V_4$ processed by selective laser melting, J. Mater. Process. Technol. 220 (2015) 202–214.
[8] D. Gu, Y.-C. Hagedorn, W. Meiners, K. Wissenbach, R. Poprawe, Selective Laser Melting of in-situ TiC/Ti_5Si_3 composites with novel reinforcement architecture and elevated performance, Surf. Coat. Technol. 205 (2011) 3285–3292.
[9] W. Frazier, Metal additive manufacturing: a review, J. Mater. Eng. Perform. 23 (2014) 1917.
[10] S.N. Dahotre, H.D. Vora, K. Pavani, R. Banerjee, An integrated experimental and computational approach to laser surface nitriding of Ti–6Al–4V, Appl. Surf. Sci. 271 (2013) 141–148.
[11] H. Chouirfa, H. Bouloussa, V. Migonney, C. Falentin-Daudré, Review of titanium surface modification techniques and coatings for antibacterial applications, Acta Biomater. 83 (2019) 37–54.
[12] B. Wysocki, P. Maj, A. Krawczyńska, K. Rożniatowski, J. Zdunek, K.J. Kurzydłowski, W. Święszkowski, Microstructure and mechanical properties investigation of CP titanium processed by selective laser melting (SLM), J. Mater. Process. Technol. 241 (2017) 13–23.
[13] H. Attar, K.G. Prashanth, A.K. Chaubey, M. Calin, L.C. Zhang, S. Scudino, J. Eckert, Comparison of wear properties of commercially pure titanium prepared by selective laser melting and casting processes, Mater. Lett. 142 (2015) 38–41.
[14] H. Attar, S. Ehtemam-Haghighi, D. Kent, I.V. Okulov, H. Wendrock, M. Bönisch, A.S. Volegov, M. Calin, J. Eckert, M.S. Dargusch, Nanoindentation and wear properties of Ti and Ti-TiB composite materials produced by selective laser melting, Mater. Sci. Eng. A 688 (2017) 20–26.
[15] I.A. Roberts, C.J. Wang, R. Esterlein, M. Stanford, D.J. Mynors, A three-dimensional finite element analysis of the temperature field during laser melting of metal powders in additive layer manufacturing, Int J Mach Tool Manu 49 (2009) 916–923.
[16] C.-W. Chan, S. Lee, G.C. Smith, C. Donaghy, Fibre laser nitriding of titanium and its alloy in open atmosphere for orthopaedic implant applications: investigations on surface quality, microstructure and tribological properties, Surf. Coat. Technol. 309 (2017) 628–640.
[17] A.M. Kamat, S.M. Copley, J.A. Todd, A two-step laser-sustained plasma nitriding process for deep-case hardening of commercially pure titanium, Surf. Coat. Technol. 313 (2017) 82–95.
[18] S. Mridha, T.N. Baker, Effects of nitrogen gas flow rates on the microstructure and properties of laser-nitrided IMI318 titanium alloy (Ti–4V–6Al), J. Mater. Process. Technol. 77 (1998) 115.
[19] R.S. Razavi, M. Salehi, M. Ramazani, H.C. Man, Corrosion behaviour of laser gas nitrided Ti–6Al–4V in HCl solution, Corros. Sci. 51 (2009) 2324–2329.
[20] H.C. Man, M. Bai, F.T. Cheng, Laser diffusion nitriding of Ti–6Al–4V for improving hardness and wear resistance, Appl. Surf. Sci. 258 (2011) 436–441.
[21] S. Sathish, M. Geetha, N.D. Pandey, C. Richard, R. Asokamani, Studies on the corrosion and wear behavior of the laser nitrided biomedical titanium and its alloys, Mater. Sci. Eng. C 30 (2010) 376–382.
[22] N. Kazantseva, N. Vinogradova, I. Ezhov, T. Kurennykh, P. Krakhmalev, I. Yadroitsev, A. Fefelov, A. Merkushev, M. Ilyinikh, Oxygen and nitrogen concentrations in the Ti-6Al-4V alloy manufactured by direct metal laser sintering (DMLS) process, Mater. Lett. 209 (2017) 311–314.
[23] S.N. Dahotre, H.D. Vora, R.S. Rajamure, L. Huang, R. Banerjee, W. He, N.B. Dahotre, Laser induced nitrogen enhanced titanium surfaces for improved osseo-integration, Ann. Biomed. Eng. 42 (2014) 50–61.
[24] G.G.E. Seward, S. Celotto, D.J. Prior, J. Wheeler, R.C. Pond, In situ SEM-EBSD observations of the hcp to bcc phase transformation in commercially pure titanium, Acta Mater. 52 (2004) 821.
[25] X. Wang, S. Zhang, X. Cheng, E. Zhu, W. Hang, B. Huang, Ion kinetic energy distributions in laser-induced plasma, Spectrochim. Acta B 99 (2014) 101–114.
[26] V. Valvoda, J. Musil, X-ray analysis of strain in titanium nitride layers, Thin Solid Films 149 (1987) 49–60.
[27] J.B. Fogagnolo, A.V. Rodrigues, E. Sallica-Leva, M.S.F. Lima, R. Caram, Surface stiffness gradient in Ti parts obtained by laser surface alloying with Cu and Nb, Surf. Coat. Technol. 297 (2016) 34–42.
[28] M.C. Biesinger, L.W.M. Lau, A.R. Gerson, R.S.C. Smart, Resolving surface chemical states in XPS analysis of first row transition metals, oxides and hydroxides: Sc, Ti, V, Cu and Zn, Appl. Surf. Sci. 257 (2010) 887–898.